

Low-dimensional dynamics of two coupled biological oscillators

Colas Droin^{ID}^{1,2}, Eric R. Paquet^{ID}^{1,2} and Felix Naef^{ID}^{1*}

The circadian clock and the cell cycle are two biological oscillatory processes that coexist within individual cells. These two oscillators were found to interact, which can lead to their synchronization. Here, we develop a method to identify a low-dimensional stochastic model of the coupled system directly from time-lapse imaging in single cells. In particular, we infer the coupling and nonlinear dynamics of the two oscillators from thousands of mouse and human single-cell fluorescence microscopy traces. This coupling predicts multiple phase-locked states showing different degrees of robustness against molecular fluctuations inherent to cellular-scale biological oscillators. For the 1:1 state, the predicted phase-shifts following period perturbations were validated experimentally. Moreover, the phase-locked states are temperature-independent and evolutionarily conserved from mouse to human, hinting at a common underlying dynamical mechanism. Finally, we detect a signature of the coupled dynamics in a physiological context, explaining why tissues with different proliferation states exhibited shifted circadian clock phases.

The circadian clock and the cell cycle are two periodic processes that cohabit in many types of living cell. In single mammalian cells, circadian clocks consist of autonomous feedback loop oscillators ticking with an average period of about 24 h (ref. ¹), and controlling many downstream cellular processes². In conditions of high proliferation such as those found in cultured cells or certain tissues, the cell cycle progresses essentially continuously and can thus be abstracted as an oscillator with an average period matching the cell doubling time. Both processes fluctuate due to intra-cell molecular noise, as well as external fluctuations. While the precision of the circadian period is typically about 15% in fibroblast cells¹, the cell cycle can be more variable depending on the conditions and cell lines^{3,4}. Interestingly, previous work showed that the two cycles can mutually interact¹, which may then lead, as theory predicts, to synchronized dynamics^{5,6} and important physiological consequences such as cell-cycle synchrony during liver regeneration⁷. In tissue-culture cells, which are amenable to systematic microscopy analysis, it was found that the phase dynamics of two oscillators shows phase-locking^{5,6}, defined by a rational rotation number $p:q$ such that p cycles of one oscillator are completed while the other completes q .

The influence of the circadian clock on cell-cycle progression and division timing has been analysed in several systems^{7–13}. On the other hand, we showed in mouse fibroblasts that the cell cycle strongly influences the circadian oscillator⁵, which was also investigated theoretically and linked with DNA replication in bacteria¹⁴. In addition, human cells can switch between a state of high cell proliferation with a damped circadian oscillator, to a state of low proliferation but robust circadian rhythms, depending on molecular interactions and activities of cell-cycle and clock regulators¹⁵.

Here, we exploit the fact that the two coupled cycles evolve on a low-dimensional and compact manifold (the flat torus) to fully characterize their dynamics. In particular, starting from a generic stochastic model for the interacting phases combined with fluorescence microscopy recordings from thousands of individual cells, we obtained a data-driven reconstruction of the coupling function describing how the cell cycle influences the circadian oscillator. This coupling phase-locks the two oscillators in a temperature-independent manner, and only a few of the determin-

istically predicted phase-locked states were stable against inherent fluctuations. Moreover, we established that the coupling between the two oscillators is conserved from mouse to human, and can override systemic synchronization signals such as temperature cycles. Finally, we showed in a physiological context how such coupling explains why mammalian tissues with different cell proliferation rates have shifted circadian phases.

Modelling the dynamics of two coupled oscillators

To study the phase dynamics of the circadian and cell-cycle oscillators, we reconstructed a stochastic dynamic model of the two coupled oscillators from single-cell time-lapse microscopy traces of a fluorescent Rev-erba-YFP (yellow fluorescent protein) circadian reporter^{1,5}. Our approach consists of explicitly modelling the measured fluorescent signals, using a set of stochastic ordinary differential equations (SODEs) whose parameters are estimated by maximizing the probability of observing the data over the entire set of cell traces (Methods). Here, we present the key components of the model (detailed in Supplementary Information).

Phase model. First, we represent the phase dynamics of the circadian oscillator ($\theta=0$ corresponds to peaks of fluorescence) and the cell cycle ($\phi=0$ represents cytokinesis) on a $[0,2\pi] \times [0,2\pi]$ torus. Since we showed previously that the influence of the clock on the cell cycle was negligible in NIH3T3 cells⁵, here we model only how the cell-cycle progression influences the instantaneous circadian phase velocity ω_θ using a general coupling function $F(\theta,\phi)$ (Fig. 1a). To account for circadian phase fluctuations and variability in circadian period length known to be present in single cells^{1,16}, we added a phase diffusion term $\sigma_\theta dW_t$. For the cell-cycle phase, we assumed a piecewise linear and deterministic phase progression in between two successive divisions. The SODEs for the phases read:

$$\begin{cases} d\theta = \frac{2\pi}{T_\theta} dt + F(\theta, \phi)dt + \sigma_\theta dW_t \\ d\phi = \frac{2\pi}{T_\phi^i} dt \end{cases} \quad (1)$$

¹Institute of Bioengineering, School of Life Sciences, Ecole Polytechnique Fédérale de Lausanne, Lausanne, Switzerland. ²These authors contributed equally: Colas Droin, Eric R. Paquet. *e-mail: felix.naef@epfl.ch

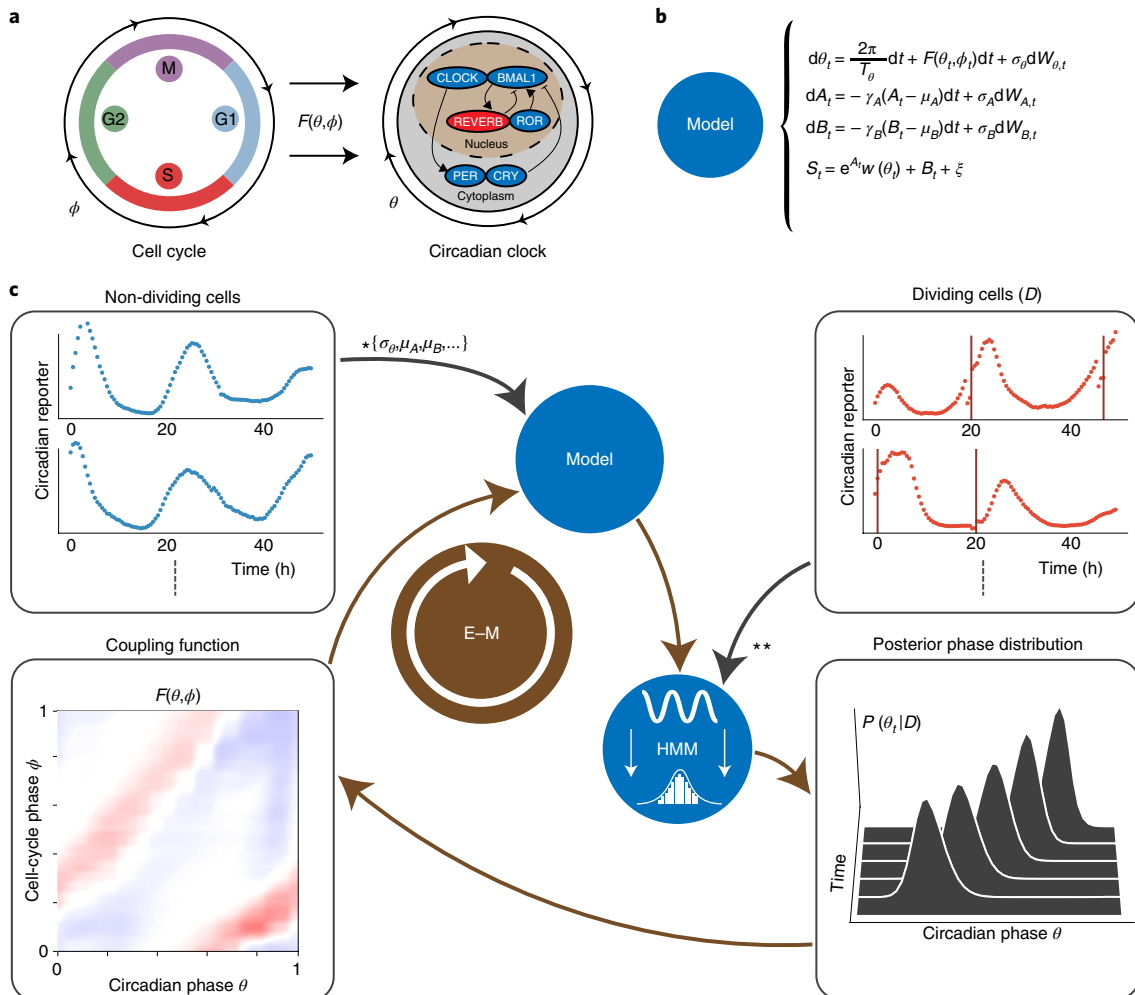


Fig. 1 | Reconstructing the phase dynamics and coupling of two biological oscillators. **a**, In mouse fibroblasts, the cell cycle (left) can influence the circadian oscillator (right) according to a coupling function $F(\theta, \phi)$, where ϕ denotes the cell cycle and θ the circadian oscillator phases. **b**, The stochastic model for the signal S_t using diffusion-drift SODEs for the circadian phase θ_t , amplitude A_t and background B_t fluctuations, as well as a function $w(\theta)$ linking the phase θ_t to the measured observations, and $F(\theta, \phi)$. **c**, Fluorescence microscopy traces (Rev-erbα-YFP circadian reporter) are recorded for non-dividing and dividing cells (top left and top right boxes). Coupling-independent parameters (*) are estimated from non-dividing cells while it is necessary to use dividing cells to infer $F(\theta, \phi)$ (**). The optimization problem is solved by converting the model to a HMM in which θ_t , A_t , and B_t are latent variables. The HMM is used on traces to compute posterior probabilities $P(\theta_t | D)$ of circadian phases (bottom right box), while the cell-cycle phase is retrieved using linear interpolation between successive divisions (top right box, vertical lines). D represents the data (all dividing cells). An iterative expectation–maximization (E–M) algorithm then yields the converged $F(\theta, \phi)$ (bottom left box).

Here, T_θ represents the intrinsic circadian period, while the term T_ϕ^i represents the i th cell-cycle interval between two successive divisions.

Model of the signal. We linked the circadian phase with the measured time traces through a 2π -periodic function $w(\theta)$. In addition, as suggested by typical data traces (Supplementary Fig. 1a), we considered amplitude (A_t) and baseline (B_t) fluctuations, which for simplicity we modelled as independent from θ_t , an assumption that was supported a posteriori (Supplementary Information). The full model for the observed signal S_t thus reads:

$$S_t = e^{A_t} w(\theta_t) + B_t + \xi \quad (2)$$

where ξ is a normally distributed random variable (measurement noise) and A_t and B_t are Ornstein–Uhlenbeck processes varying more slowly than the phase distortion caused by $F(\theta, \phi)$

(that is, on timescales on the order of the circadian period; Supplementary Information).

Inference of phases and coupling function. From this stochastic model (equations (1) and (2), Fig. 1b), we built a hidden Markov model (HMM) to calculate posterior probabilities of the oscillator phases at each measured time point, using the forward–backward algorithm¹⁷. To estimate $F(\theta, \phi)$, we used a maximum-likelihood approach that combines goodness of fit with sparseness and smoothness constraints, which we implemented with an expectation–maximization algorithm (Methods and Supplementary Information).

The successive steps of our approach are illustrated in Fig. 1c. The traces of dividing cells indicated that, typically, the circadian phase progression shows variations in phase velocity (Supplementary Fig. 1a). To validate that these variations can be used to identify $F(\theta, \phi)$, we generated noisy traces in silico with predefined $F(\theta, \phi)$ and

reconstructed the coupling function, showing excellent qualitative agreement (Supplementary Fig. 1b,c).

Influence of the cell cycle on the circadian phase

In mouse embryonic fibroblasts (NIH3T3), we showed that due to the coupling, circadian periods decrease with temperature in dividing cells, but not in quiescent cells⁵. To further understand how temperature influences the interaction between the two oscillators, we reanalysed NIH3T3 traces (24–72 h long) obtained at 34 °C, 37 °C, and 40 °C (ref. ⁵). From those, we found that both the inferred coupling functions and phase densities at the three temperatures were very similar, with almost identical 1:1 phase-locked orbits (Supplementary Fig. 2a–c). We therefore modelled the coupling as temperature-independent and reconstructed a definitive $F(\theta, \phi)$ from traces at all temperatures (Fig. 2a and Supplementary Fig. 2d). This function shows a diffuse structure mainly composed of two juxtaposed diagonal stripes: one for phase acceleration (red) and one, less structured, for deceleration (blue). The slopes of these stripes are about 1, which indicates that an approximate minimal model of the coupling would be a function $F(\theta, \phi) = f(\theta - \phi)$. However, the phase velocity varies along the stripes and attractor (see below), which justifies using a two-dimensional parameterization of the coupling function. The phase density for cells with fixed cell-cycle period of 22 h (corresponding to the mean cell-cycle period in the full dataset; Fig. 2b and Supplementary Video 1) clearly suggests 1:1 phase-locking. In fact, analysing the predicted deterministic dynamics (equation (1), with the reconstructed $F(\theta, \phi)$, and without the noise) shows a 1:1 attractor (Fig. 2c). Thus, in this 1:1 state, the endogenous circadian period of 24 h is shortened by 2 h, which results from acceleration occurring after cytokinesis ($\phi = 0$ when the circadian phase is near $\theta \approx 0.8 \times 2\pi$, and lasting for the entire G1 phase, until about $\theta \approx 0.4 \times 2\pi$ when cells typically enter S phase ($\phi \approx 0.4 \times 2\pi$ at the G1/S transition; Supplementary Information and Fig. 2d).

Phase dynamics in perturbation experiments

The reconstructed model allows us to simulate the circadian phase dynamics as a function of the cell-cycle period, which is relevant as the cells display a significant range of cell-cycle lengths (Supplementary Fig. 3a). In the deterministic system, we find 1:1 phase-locking over a range of cell-cycle times varying from 19 h to 27 h, showing that the cell cycle can both globally accelerate and slow down circadian phase progression (Fig. 3a). The attractor shifts progressively to the right in the phase space, yielding a circadian phase at division ranging from $\theta \approx 0.7 \times 2\pi$ when $T_\phi = 19$ h to $\theta \approx 0.9 \times 2\pi$ when $T_\phi = 27$ h. Since the attractor for different cell-cycle periods shifts, the circadian phase velocity profile also changes (Supplementary Fig. 3b). To validate the predicted shifts, we experimentally subjected cells to perturbations inducing a large variety of cell-cycle periods and compared the observed circadian phase to the model prediction at three different cell-cycle phases, revealing an excellent agreement, with no additional free parameters (Fig. 3b).

The simulations also clearly revealed multiple phase-locked states (1:2, 1:1, 2:1, 3:1 and so on, with $p:q$ indicating the number of cell cycles p and the number of clock cycles q), represented as Arnold tongues (Fig. 3c, and Supplementary Video 2 for an animated phase-space representation). We identified cell data trajectories following almost perfectly the deterministic attractors, both in the 1:1 and 1:2 phase-locking states (Fig. 3e,f, respectively); however, cells showing other $p:q$ states were rarely observed.

Fluctuations extend 1:1 phase-locking asymmetrically

To understand the differences between the simulated deterministic system and observed cell traces, we simulated the stochastic dynamics (equation (1)). We then compared measured data trajectories stratified by cell-cycle periods (Fig. 4a) with deterministic (Fig. 4b)

and stochastic simulations (Fig. 4c). This revealed that data agree better with stochastic than deterministic simulations, indicating that the phase fluctuations qualitatively change the phase portrait. One striking observation is the increased range of 1:1 phase-locking in the noisy system; however, the extension is asymmetric, as it occurs for shorter, but not for longer, cell-cycle periods. Indeed, while 1:2 phase-locking is observed in the data and the noisy simulations, the deterministically predicted 2:1 state is replaced in the data and stochastic system by 1:1-like orbits. Consistently, spectral analysis revealed significant differences between deterministic and stochastic simulations (Supplementary Fig. 4a,b and Supplementary Video 3); in addition, the coupling, specifically in the 1:1 state, was able to efficiently filter the noise (Supplementary Fig. 4b, right).

Evolutionarily conserved phase-locking

Most studies investigating the interaction between the cell cycle and the circadian oscillators in mammals are based on rodent models^{1,5–8,18}. To test whether the above phase-locked dynamics are conserved in human U2OS cells, an established circadian oscillator model^{19,20}, we engineered a U2OS cell line termed U2OS-Dual expressing a dual circadian fluorescent (Rev-erbα-YFP) and luminescent (Bmal1-Luc) reporter system. U2OS-Dual cells possess a functional circadian clock behaving similarly to NIH3T3 cells also expressing a Bmal1-Luc luminescent reporter²¹ (Fig. 5a). We scrutinize the relation between the two cell lines by comparing their behaviour in different conditions: at 34 °C and 37 °C for cells with synchronized and non-synchronized circadian cycles⁵ (Fig. 5b–g).

Similarly to NIH3T3 cells, the division events of non-synchronized U2OS-Dual cells grown at 37 °C occurred 4.96 ± 2.6 h before a peak in the circadian fluorescent signal (Fig. 5c), indicating that the cell cycle and the circadian clock interact. To investigate the directionality of this interaction, we tested, as in NIH3T3 cells⁵, whether the circadian clock phase could influence cell-cycle progression by resetting the circadian oscillator using dexamethasone, a circadian resetting cue²² that does not perturb the cell cycle¹. The expected resetting effect of dexamethasone on the circadian phase is indicated by the density of peaks in reporter levels during the first 10 h of recording, but with unnoticeable effects on the timing of the first division (Fig. 5d). However, the circadian peak following the first division occurred systematically around 5 h after the division in both conditions, suggesting that cell division in U2OS can reset circadian phases and overwrite dexamethasone synchronization. Synchronization of the circadian clocks for dexamethasone- versus non-treated cells was expectedly higher for dexamethasone and gradually decreased to reach the level of the untreated cells (Fig. 5e), contrasting with the generally lower synchronization of cell divisions in both conditions. To then test whether the cell cycle could influence the circadian clock, we lengthened the cell-cycle period by growing cells at 34 °C and compared their behaviour with those grown at 37 °C. Interestingly, cells at 34 °C showed a longer circadian period compared to those at 37 °C (Fig. 5f), unlike the temperature-compensated circadian periods (~25 h) in non-dividing cells (Fig. 5a,g,h).

Thus, similarly to mouse NIH3T3 cells, the coupling directionality is predominantly from the cell cycle to the circadian clock. In fact, the reconstructed coupling function for U2OS-Dual cells grown at 37 °C (Fig. 5i) is structurally similar to that obtained in mouse fibroblasts (Fig. 2a), with the ensuing dynamics also showing a 1:1 attractor.

Dividing cells lose circadian temperature entrainment

In mammals, circadian clocks in tissues are synchronized by multiple systemic signals²³. In fact, temperature oscillations mimicking those physiologically observed can phase-lock circadian oscillators in non-dividing (contact-inhibited) NIH3T3 cells *in vitro*²⁴. To study how the observed interactions influence temperature entrainment,

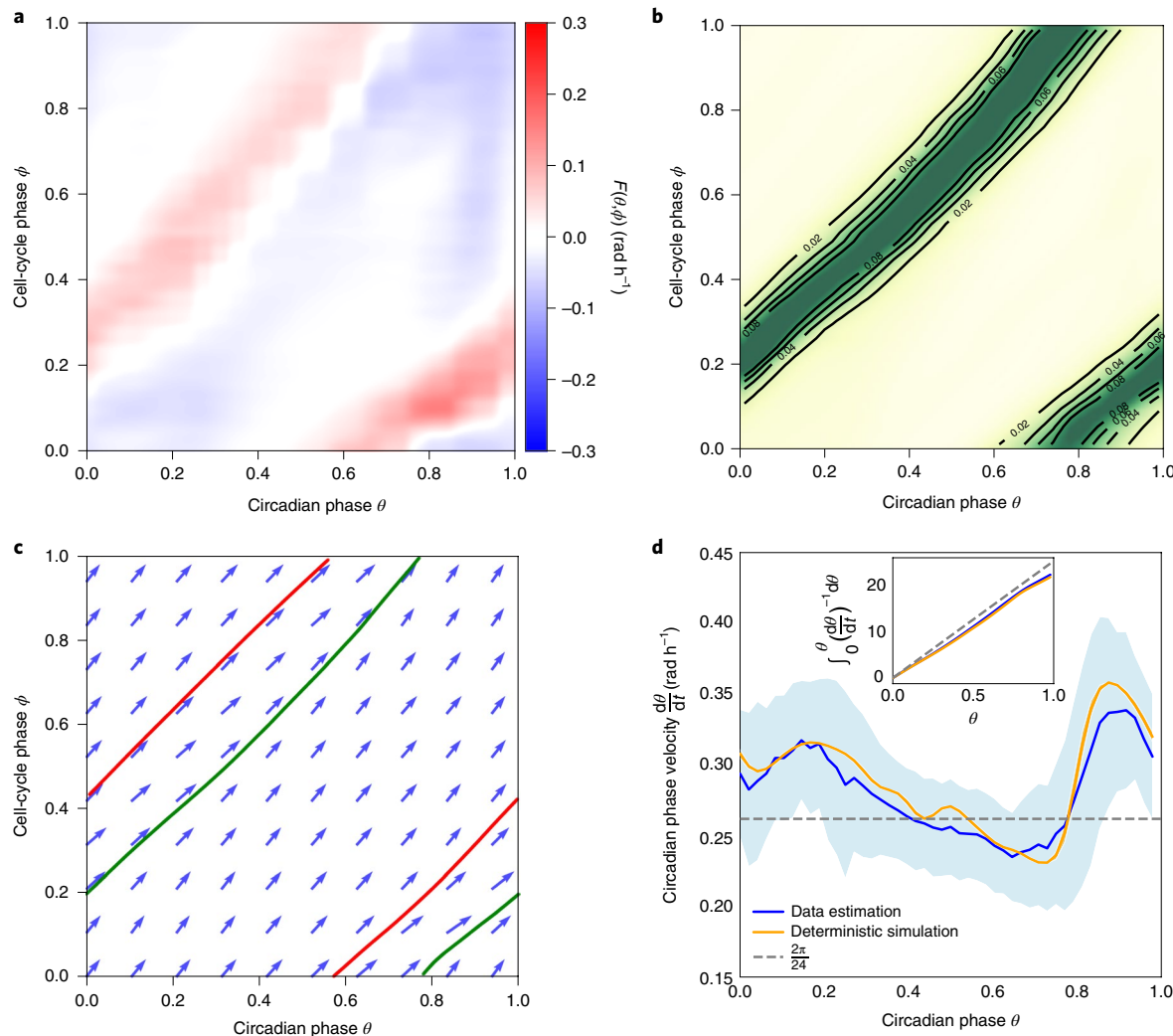


Fig. 2 | Influence of the cell cycle on the circadian phase enables 1:1 phase-locking. **a**, Coupling $F(\theta, \phi)$ optimized on dividing single-cell traces. Due to the similar results (Supplementary Fig. 2), traces from the three temperatures ($n=154$, 271 and 302 traces at 34 °C, 37 °C and 40 °C, respectively) are pooled. **b**, The density of inferred phase traces from all of the dividing traces with 22 ± 1 h cell-cycle intervals indicates a 1:1 phase-locked state. **c**, Numerical integration of the phase velocity field (arrows, deterministic model) yields 1:1 attractor (green line) and repeller (red line). Here, the cell-cycle period was set to 22 h. **d**, The circadian phase velocity is not constant along the attractor, here for cells with 22 ± 1 h cell-cycle intervals. Data (blue line, standard deviation in light-blue shading) and deterministic simulation (orange line). Inset: integrated time along the attractor. The grey line shows constant bare phase velocity $\omega_0 = \frac{2\pi}{24h}$.

we applied temperature cycles (24 h period ranging from 35.5 °C to 38.5 °C) to U2OS cells growing at different rates (plated at different densities) and monitored population-wide Bmal1–Luc signals (Fig. 6a). We found that, independently of initial densities, as the populations reach confluence, the phases and amplitudes become stationary, showing 1:1 entrainment (Fig. 6b,c and Supplementary Fig. 5a). During the initial transients, emerging circadian oscillations in non-confluent cells showed phases that were already stationary, at least once cell numbers were sufficiently high to obtain reliable signals.

As the cell confluence increases, the proportion of cells that stop cycling (exit to G0) increases²⁵. We therefore hypothesized that the observed phase and amplitude profiles in Bmal1–Luc signals (Fig. 6b,c) originate from a mixture of two populations: an increasing population of non-dividing cells (G0) showing ‘normal’ entrainment properties, and dividing cells. We considered three scenarios for the dividing cells: the circadian oscillators in dividing cells adopt the same circadian profile as non-dividing entrained cells; are not entrained; or are entrained, but with a different phase compared to

non-dividing cells (Supplementary Fig. 5b). These scenarios can be distinguished by the predicted phase and amplitude profiles (Supplementary Fig. 5c). Clearly, the measured profiles for U2OS-Dual cells favoured the second scenario, suggesting that circadian oscillators in dividing cells do not entrain to the applied temperature cycles.

Proliferation is associated with tissue-specific phases

The above findings suggest that phases or amplitudes of circadian clocks in organs *in vivo* might be influenced by the proliferation state of cells in the tissue. To test this, we investigated circadian clock parameters in different mouse tissues using a study of mRNA levels in 12 adult (6-week-old males) mouse tissues, which revealed that clock phases span 1.5 h between the earliest and latest tissues (Fig. 6d)^{26,27}, an effect that is considered large in chronobiology as even period phenotypes of core clock genes are often smaller^{2,28,29}. We noticed that the mean mRNA levels across tissues of many genes correlated with the phase offsets (Supplementary Table 1). However, gene functions related to cell proliferation stood out as the most

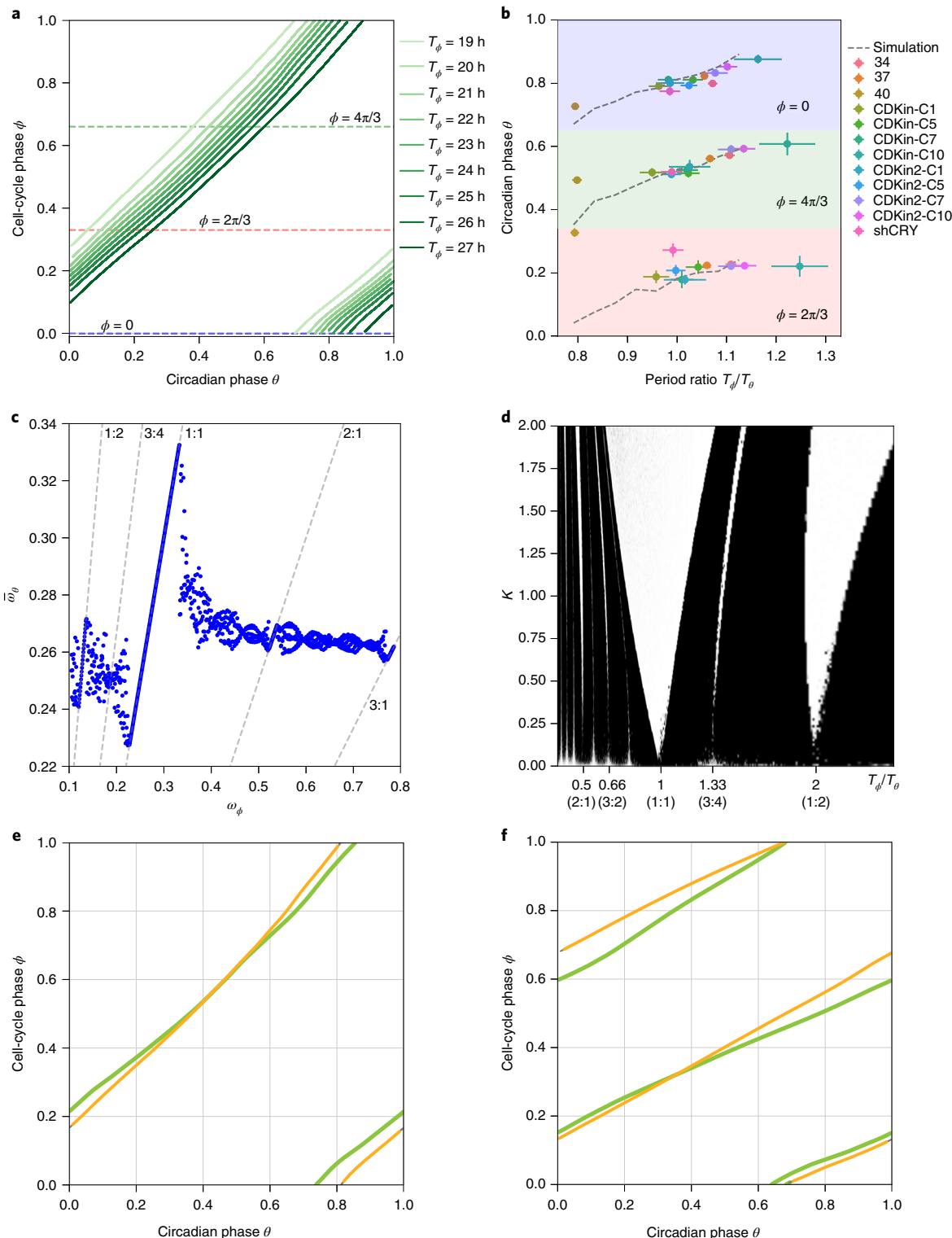


Fig. 3 | The coupling between the cell cycle and the circadian oscillator predicts phase-shifts and phase-locking attractors in perturbation experiments.

a, Simulated (deterministic) attractors for cell-cycle periods ranging from 19 h to 27 h show that the dephasing of the cell cycle and the circadian oscillator changes within the 1:1 state. Periods just outside this range yield quasiperiodic orbits. The horizontal dashed lines indicate three different cell-cycle phases $\phi = 0$, $\phi = \frac{2}{3} \times 2\pi$, $\phi = \frac{4}{3} \times 2\pi$ used in **b**. **b**, Predictions from **a** (dashed grey lines) against independent experimental data collected from 12 perturbation experiments (coloured symbols, see legend, notation explained in Methods). shCRY, shRNA-mediated knockdown of Cry2. **c**, Multiple phased-locked states are predicted, recognizable by rational relationships between the frequencies of the entraining cell cycle and the entrained circadian oscillator, interspersed with quasiperiodic intervals. **d**, Arnold tongues showing multiple phase-locked states as a function of cell-cycle periods and coupling strength ($K=1$ corresponds to the experimentally found coupling). Stable zones (white tongues) reveal attractors interspersed by quasiperiodicity. Although there are only two wider phased-locked states (1:1 and 1:2), several other $p:q$ states are found. **e,f**, Representative single-cell traces (data in yellow) evolving near predicted attractors (green lines). The traces are for a cell with $T_\phi = 24$ h (**e**) and one with $T_\phi = 48$ h (**f**) near the 1:1 and 1:2 orbits, respectively.

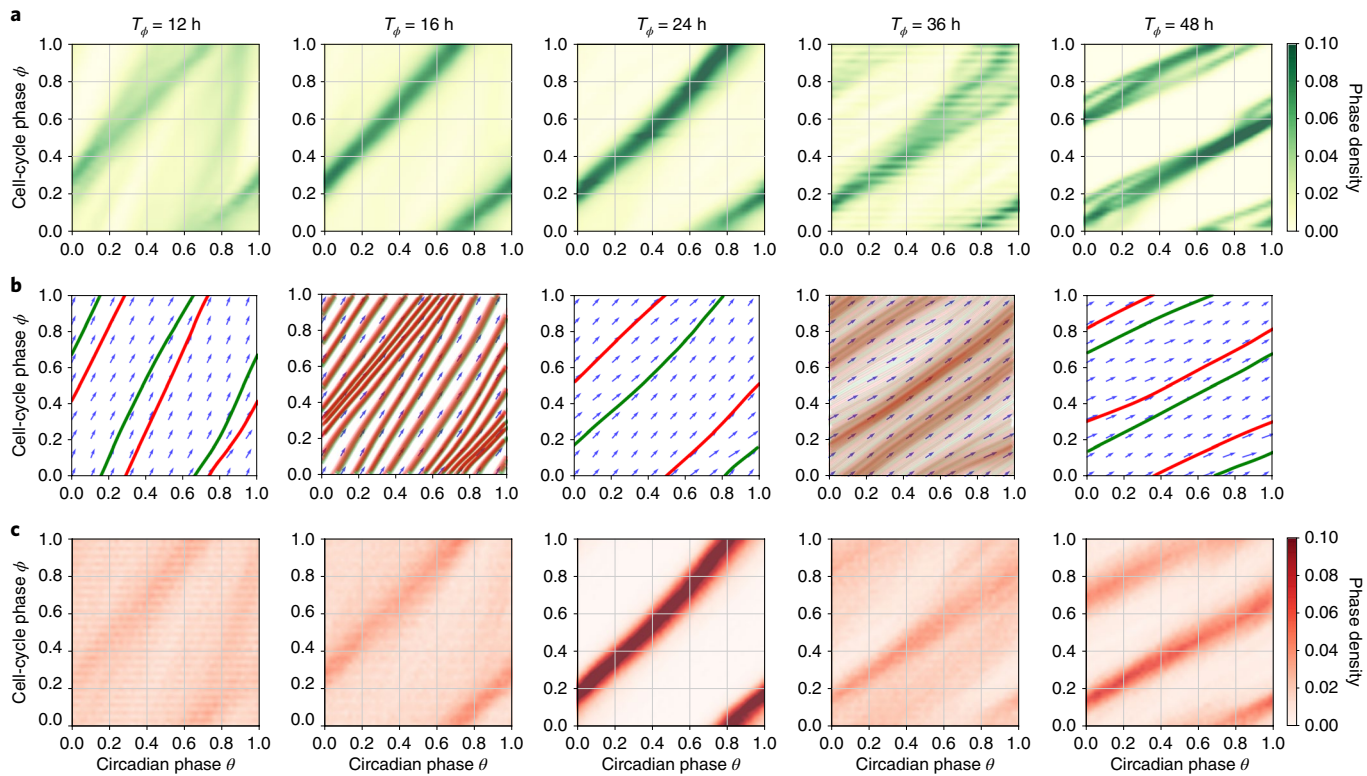


Fig. 4 | Single-cell data and stochastic simulations reveal robust 1:1 and 1:2 phase-locked states. **a**, Phase-space densities from the experimental traces stratified by cell-cycle periods (± 1 h for each reference period); $n=16, 223, 303, 54$ and 4 cell traces in the $T=12, 16, 24, 36$ and 48 h panels, respectively. **b**, Vector fields and simulated (deterministic) trajectories for the different cell-cycle periods. Attractors are shown in green (forward time integration) and repellers (backward integration) in red (see also Supplementary Video 2). **c**, Phase-space densities obtained from stochastic simulations of the model match better with the data compared to **b**.

strongly enriched (Fig. 6f and Supplementary Table 1). Among those genes, the levels of known markers of cell proliferation such as *Mki67* or *Myc* were strongly correlated with the phase offsets (Fig. 6g,h and Supplementary Table 1). Amplitudes, on the other hand, were not correlated with proliferation genes, but rather with neuronal specific genes, as expected owing to the damped rhythms present in those tissues (Fig. 6i and Supplementary Table 1)²⁶. Thus, this analysis suggests that the differences in basal proliferation levels observed in normal tissues might underlie the dephasing of the circadian clock, suggesting a physiological role for the interaction of the cell cycle and circadian clocks.

Discussion

A goal in quantitative single-cell biology is to obtain data-driven and dynamical models of biological phenomena in low dimensions. In practice, the heterogeneity and complex physics underlying the emergence of biological function in non-equilibrium living systems, as well as the sparseness of available measurements, pose challenges. Here, we studied a system of two coupled biological oscillators, sufficiently simple to allow data-driven model identification, yet complex enough to exhibit qualitatively distinct dynamics (that is, p:q states and quasiperiodicity).

In the coupled cell-cycle and circadian oscillator system, phase-locked states different from 1:1 have been observed¹⁰. While multiple attractors, notably 1:1 and 3:2, were found in mouse NIH3T3 cells under transient dexamethasone stimulation⁶, here we report 1:2 states for long cell-cycle times under steady, unstimulated, conditions. Unlike other deterministically predicted states, 1:2 was sufficiently robust and observed in some cells. In fact, we found that noise extended the range of the 1:1 tongue, but asymmetrically (that

is, towards decreased cell-cycle periods). This may be reminiscent of generalized Poincaré oscillators showing that the entrainment range is broader for limit cycles with low relaxation rates³⁰. Indeed, noise could decrease relaxation rates and thereby broaden Arnold tongues. In addition, for certain cell-cycle periods, we observed the superposition of multiple states, both in the data and in the stochastic simulations, but not in the deterministic analysis (Fig. 4, see notably $T=12$ h and $T=36$ h). This is reminiscent of mode hopping as described in the context of an oscillatory gene circuit underlying inflammatory responses³¹; however, here the corresponding Arnold tongues do not overlap in the range of the biologically relevant coupling strength ($K=1$, Fig. 3d).

While we focused on the emergent dynamics in the coupled oscillator system, considerations on possible biological mechanisms are relevant for follow-up biochemical analyses. How chromosome condensation or nuclear envelope breakdown may influence the circadian clock phase progression via either transcriptional shutdown or displacement of chromatin-bound circadian repressors, respectively, was discussed previously⁵. For example, *Rev-erba* transcription being so tightly locked to cell divisions (the peak accumulation of the reporter occurs 5 h after mitosis) could reflect the sudden derepression of its promoter, due to a displaced CRYPTOCHROME1 (CRY1)-containing repressor complex following nuclear envelope breakdown³². In turn, REV-ERB-A accumulation influences the clock phase by binding to promoters of multiple core clock components, including *Cry1*^{33,34}. More specific transcriptional activities could also play a key role in coupling the cell and circadian cycles. In fact, the circadian oscillator is exquisitely sensitive to numerous signalling pathways, impinging on the clock by transcriptional induction of *Period* genes, which thus provides an efficient

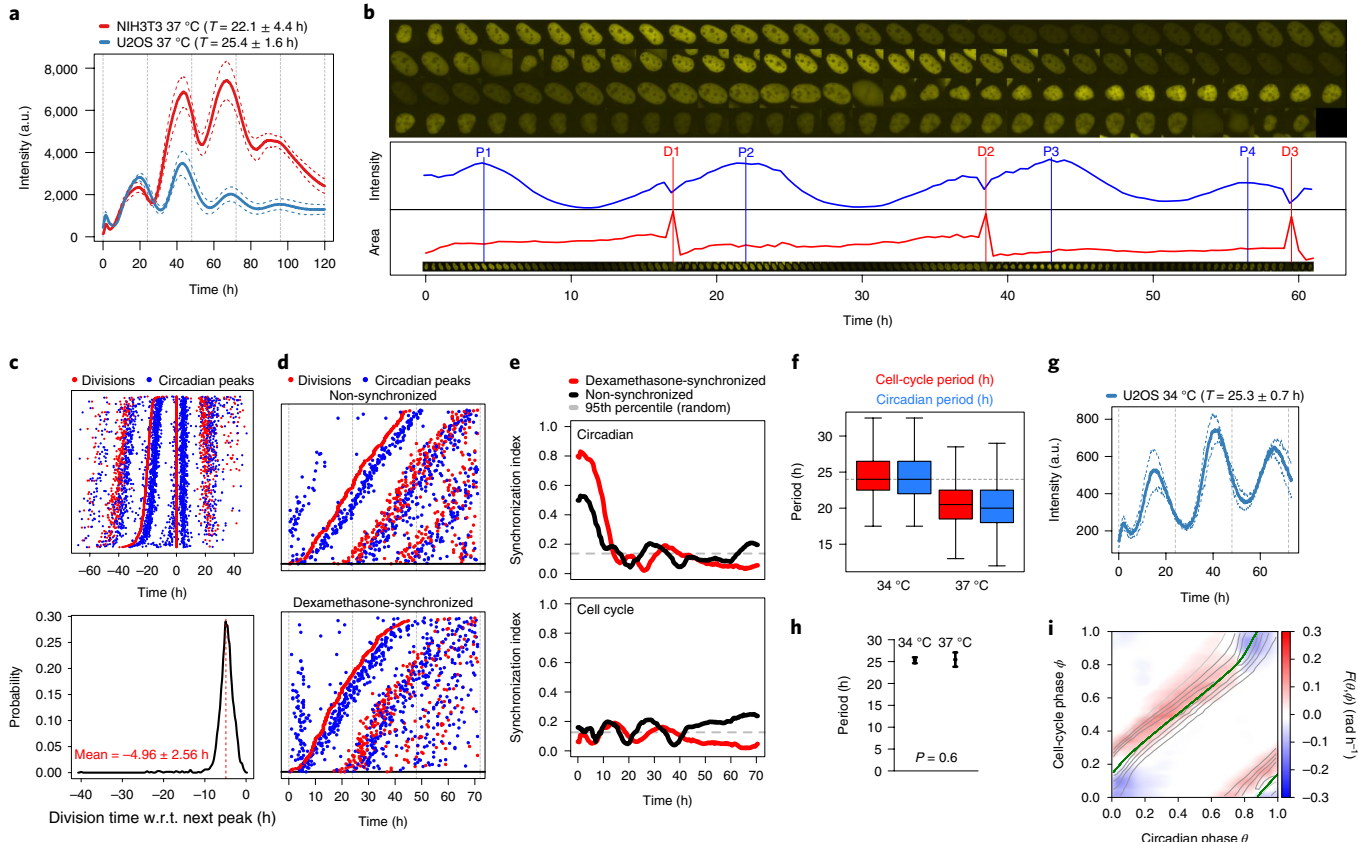


Fig. 5 | Conserved influence of the cell cycle on the circadian clock in human U2OS osteosarcoma cells. **a**, Mean luminescence intensities (\pm s.d., $n=3$) from non-dividing NIH3T3 and U2OS cells grown at 37 °C expressing a Bmal1-Luc reporter. The values in the legend correspond to the mean periods \pm s.d. **b**, Top: semi-automated tracking of U2OS cell lines expressing the Rev-erb α -YFP circadian fluorescent reporter. Bottom: circadian traces obtained from quantification of tracked nuclei. The red vertical lines represent cell divisions (cytokinesis) and the blue vertical lines show Rev-erb α -YFP signal peaks. **c**, Top: stack of divisions (red) and Rev-erb α -YFP peaks (blue) for U2OS single-cell traces centred on divisions. Bottom: distribution of the time of division relative to the next Rev-erb α -YFP peaks (in red; mean \pm s.d., $n=1,298$). **d**, Divisions and Rev-erb α -YFP peaks from single non-synchronized (top), and dexamethasone-synchronized (bottom) U2OS traces ordered on the first division. **e**, The synchronization index from non-synchronized (black) and dexamethasone-synchronized (red) traces for the circadian phase (top) and cell-cycle phase (bottom) estimated as in ref. ⁵. The circadian synchronization index from non-synchronized cells is relatively high due to plating. The dashed grey lines show the 95th percentiles of the synchronization index for randomly shuffled traces. **f**, Cell-cycle and circadian periods for U2OS cells grown at 34 °C and 37 °C ($n > 90$ for all distributions). **g**, Mean luminescence intensities (\pm s.d., $n=3$) for non-dividing U2OS cells grown at 34 °C expressing a Bmal1-Luc reporter. The values in the legend correspond to the mean periods \pm s.d. **h**, Mean and standard deviation of the circadian period for non-dividing U2OS cells grown at 34 °C and 37 °C ($n=8$ at 34 °C and $n=9$ at 37 °C, two-sided Wilcoxon's test). **i**, The coupling function $F(\theta, \phi)$ optimized on $n=551$ dividing U2OS cells grown at 37 °C, superimposed with the attractor ($T_\phi=22$ h) obtained from deterministic simulations (green line).

synchronization method²². Similarly, entrainment via temperature cycles also converges onto *Period* gene transcription²⁴. However, we are not aware of cell-cycle-dependent transcriptional regulators, such as E2F factors, targeting clock components such as the *Period* genes. Finally, since the regulation of protein stability is important for clock function³⁵, it is possible that phosphorylation-controlled proteolytic activities driving the cell cycle could target circadian phase regulators³⁶, thereby mediating the observed coupling.

In mammals, the circadian oscillator in the suprachiasmatic nucleus is the pacemaker for the entire organism³⁷, driving 24 h rhythms in activity, feeding, body temperature and hormone levels. In particular, the suprachiasmatic nucleus can synchronize peripheral cell-autonomous circadian clocks located within organs across the body³⁸. Consistent with theory³⁹, in a physiological context of entrainment, the coupling of the cell cycle with the circadian clock can induce proliferation-dependent phase-shifts, which we observed. Such phase-shifts could reflect a homogeneous behaviour of all cells, or it could reflect heterogeneity of

cell proliferation states, possibly leading to wave propagation. The phase-shifts we observed in tissues were associated with low proliferation (that is, non-pathological states of tissue homeostasis and cell renewal). For example, the liver and the adrenal gland showed a phase advance compared to fully quiescent tissues such as the brain.

When cell proliferation is abnormally high such as in cancer, circadian clocks are often severely damped⁴⁰. While this absence of a robust circadian rhythm in malignant tissue states may reflect non-functional circadian oscillators due to mutations in clock genes⁴¹, the damped rhythms may also reflect circadian desynchrony of otherwise functional circadian oscillators. Such desynchrony would readily follow from the coupling between the cell-cycle and circadian oscillators we highlight here, in the presence of non-coherent cell-cycle progression.

Methodologically, the new approach to reconstruct a dynamical model for the coupled oscillator system has significant advantages over previous methods; notably, strong assumptions such as

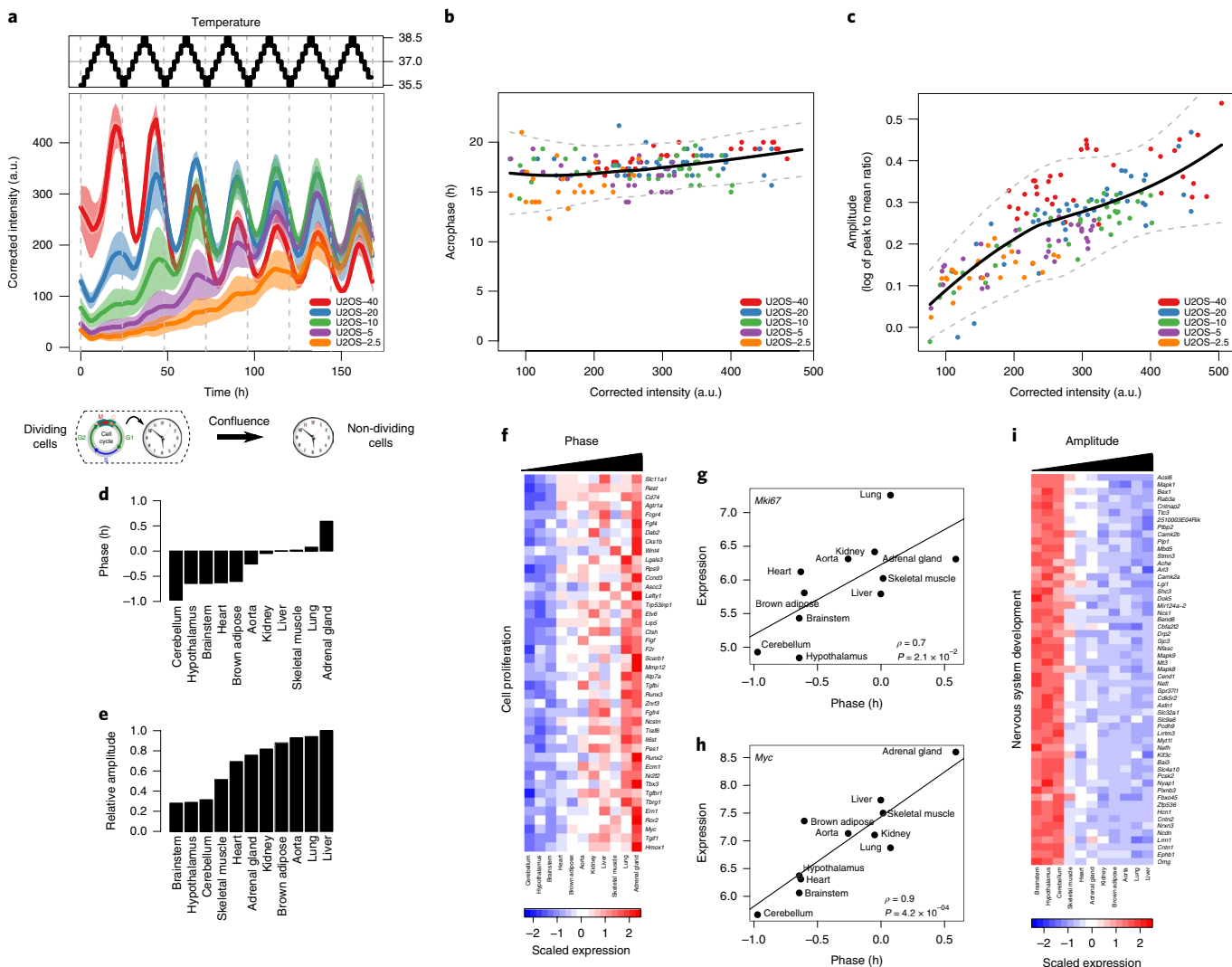


Fig. 6 | Temperature cycles do not entrain circadian oscillators in dividing cells and proliferation genes are associated with tissue-specific circadian phases. **a**, Corrected and averaged Bmal1-Luc intensities and 95% confidence intervals ($n=6$) from U2OS-Dual cells plated at different initial densities and subjected to a temperature entrainment (top). **b**, Acrophases (times of the local peaks in luminescence) of the Bmal1-Luc signal as a function of the reporter intensity for the cells in **a**. Loess fit (black) and 95% confidence intervals (grey). **c**, Amplitude (log of peak to mean ratio) of the Bmal1-Luc oscillations as a function of the reporter intensity for the cells in **a**. Loess fit (black) and 95% confidence intervals (grey). **d,e**, Circadian phases (**d**) and amplitudes (**e**) of different mouse tissues obtained in ref. ²⁷, relative to liver. **f**, Expression levels of genes positively associated with phases from **d** and linked to cell proliferation. **g,h**, Correlations between Mki67 (**g**) and Myc (**h**) mRNA expression and circadian phases across mouse tissues (Pearson's correlation, two-sided P values from a t -distribution with $n-2$ degrees of freedom). **i**, Expression levels of genes negatively associated with amplitudes and linked to nervous system development.

the sparse and localized coupling are dispensable⁵. Compared with generic model identification techniques⁴², our approach models the raw data and its noise structure explicitly. In the future, such data-driven identification of dynamical models might reveal dynamical instabilities underlying ordered states in spatially extended systems, as occurring, for instance, during somitogenesis⁴³.

Online content

Any methods, additional references, Nature Research reporting summaries, source data, statements of code and data availability and associated accession codes are available at <https://doi.org/10.1038/s41567-019-0598-1>.

Received: 5 February 2019; Accepted: 18 June 2019;
Published online: 5 August 2019

References

1. Nagoshi, E. et al. Circadian gene expression in individual fibroblasts: cell-autonomous and self-sustained oscillators pass time to daughter cells. *Cell* **119**, 693–705 (2004).
2. Mermet, J., Yeung, J. & Naeff, F. Systems chronobiology: global analysis of gene regulation in a 24-hour periodic world. *Cold Spring Harb. Perspect. Biol.* **9**, <https://doi.org/10.1101/cshperspect.a028720> (2017).
3. Hahn, A. T., Jones, J. T. & Meyer, T. Quantitative analysis of cell cycle phase durations and PC12 differentiation using fluorescent biosensors. *Cell Cycle* **8**, 1044–1052 (2009).
4. Spencer, S. L. et al. The proliferation–quiescence decision is controlled by a bifurcation in CDK2 activity at mitotic exit. *Cell* **155**, 369–383 (2013).
5. Bieler, J. et al. Robust synchronization of coupled circadian and cell cycle oscillators in single mammalian cells. *Mol. Syst. Biol.* **10**, 739 (2014).
6. Feillet, C. et al. Phase locking and multiple oscillating attractors for the coupled mammalian clock and cell cycle. *Proc. Natl Acad. Sci. USA* **111**, 9828–9833 (2014).

7. Matsuo, T. et al. Control mechanism of the circadian clock for timing of cell division in vivo. *Science* **302**, 255–259 (2003).
8. Kowalska, E. et al. NONO couples the circadian clock to the cell cycle. *Proc. Natl Acad. Sci. USA* **110**, 1592–1599 (2013).
9. Mori, T., Binder, B. & Johnson, C. H. Circadian gating of cell division in cyanobacteria growing with average doubling times of less than 24 hours. *Proc. Natl Acad. Sci. USA* **93**, 10183–10188 (1996).
10. Yang, Q., Pando, B. F., Dong, G., Golden, S. S. & van Oudenaarden, A. Circadian gating of the cell cycle revealed in single cyanobacterial cells. *Science* **327**, 1522–1526 (2010).
11. Matsu-Ura, T. et al. Intercellular coupling of the cell cycle and circadian clock in adult stem cell culture. *Mol. Cell* **64**, 900–912 (2016).
12. Plikus, M. V. et al. Local circadian clock gates cell cycle progression of transient amplifying cells during regenerative hair cycling. *Proc. Natl Acad. Sci. USA* **110**, E2106–E2115 (2013).
13. Gerard, C. & Goldbeter, A. Entrainment of the mammalian cell cycle by the circadian clock: modeling two coupled cellular rhythms. *PLoS Comput. Biol.* **8**, e1002516 (2012).
14. Pajjmans, J., Bosman, M., Ten Wolde, P. R. & Lubensky, D. K. Discrete gene replication events drive coupling between the cell cycle and circadian clocks. *Proc. Natl Acad. Sci. USA* **113**, 4063–4068 (2016).
15. Shostak, A. et al. MYC/MIZ1-dependent gene repression inversely coordinates the circadian clock with cell cycle and proliferation. *Nat. Commun.* **7**, 11807 (2016).
16. Rougemont, J. & Naef, F. Collective synchronization in populations of globally coupled phase oscillators with drifting frequencies. *Phys. Rev. E* **73**, 011104 (2006).
17. Rabiner, L. R. & Juang, B.-H. An introduction to hidden Markov models. *IEEE ASSP Mag.* **3**, 4–16 (1986).
18. Yeom, M., Pendergast, J. S., Ohmiya, Y. & Yamazaki, S. Circadian-independent cell mitosis in immortalized fibroblasts. *Proc. Natl Acad. Sci. USA* **107**, 9665–9670 (2010).
19. Vollmers, C., Panda, S. & DiTacchio, L. A high-throughput assay for siRNA-based circadian screens in human U2OS cells. *PLoS One* **3**, e3457 (2008).
20. Maier, B. et al. A large-scale functional RNAi screen reveals a role for CK2 in the mammalian circadian clock. *Genes Dev.* **23**, 708–718 (2009).
21. Nicolas, D., Zoller, B., Suter, D. M. & Naef, F. Modulation of transcriptional burst frequency by histone acetylation. *Proc. Natl Acad. Sci. USA* **115**, 7153–7158 (2018).
22. Balsalobre, A. et al. Resetting of circadian time in peripheral tissues by glucocorticoid signaling. *Science* **289**, 2344–2347 (2000).
23. Dibner, C., Schibler, U. & Albrecht, U. The mammalian circadian timing system: organization and coordination of central and peripheral clocks. *Annu. Rev. Physiol.* **72**, 517–549 (2010).
24. Saini, C., Morf, J., Stratmann, M., Gos, P. & Schibler, U. Simulated body temperature rhythms reveal the phase-shifting behavior and plasticity of mammalian circadian oscillators. *Genes Dev.* **26**, 567–580 (2012).
25. Hayes, O. et al. Cell confluence is as efficient as serum starvation for inducing arrest in the G0/G1 phase of the cell cycle in granulosa and fibroblast cells of cattle. *Anim. Reprod. Sci.* **87**, 181–192 (2005).
26. Zhang, R., Lahens, N. F., Ballance, H. I., Hughes, M. E. & Hogenesch, J. B. A circadian gene expression atlas in mammals: implications for biology and medicine. *Proc. Natl Acad. Sci. USA* **111**, 16219–16224 (2014).
27. Yeung, J. et al. Transcription factor activity rhythms and tissue-specific chromatin interactions explain circadian gene expression across organs. *Genome Res.* **28**, 182–191 (2018).
28. Cermakian, N., Monaco, L., Pando, M. P., Dierich, A. & Sassone-Corsi, P. Altered behavioral rhythms and clock gene expression in mice with a targeted mutation in the Period1 gene. *EMBO J.* **20**, 3967–3974 (2001).
29. Debruyne, J. P. et al. A clock shock: mouse CLOCK is not required for circadian oscillator function. *Neuron* **50**, 465–477 (2006).
30. Granada, A. E. & Herzel, H. How to achieve fast entrainment? The timescale to synchronization. *PLoS One* **4**, e7057 (2009).
31. Heltberg, M., Kellogg, R. A., Krishna, S., Tay, S. & Jensen, M. H. Noise induces hopping between NF-κB entrainment modes. *Cell Syst.* **3**, 532–539 e533 (2016).
32. Aryal, R. P. et al. Macromolecular assemblies of the mammalian circadian clock. *Mol. Cell* **67**, 770–782.e6 (2017).
33. Ukai-Tadenuma, M. et al. Delay in feedback repression by cryptochrome 1 is required for circadian clock function. *Cell* **144**, 268–281 (2011).
34. Mermet, J. et al. Clock-dependent chromatin topology modulates circadian transcription and behavior. *Genes Dev.* **32**, 347–358 (2018).
35. Siepka, S. M. et al. Circadian mutant overtime reveals F-box protein FBXL3 regulation of cryptochrome and period gene expression. *Cell* **129**, 1011–1023 (2007).
36. King, R. W., Deshaies, R. J., Peters, J. M. & Kirschner, M. W. How proteolysis drives the cell cycle. *Science* **274**, 1652–1659 (1996).
37. Hastings, M. H., Maywood, E. S. & Brancaccio, M. Generation of circadian rhythms in the suprachiasmatic nucleus. *Nat. Rev. Neurosci.* **19**, 453–469 (2018).
38. Mohawk, J. A., Green, C. B. & Takahashi, J. S. Central and peripheral circadian clocks in mammals. *Annu. Rev. Neurosci.* **35**, 445–462 (2012).
39. Pikovsky, A. R. M. K. J. *Synchronization* (Cambridge University Press, 2001).
40. Shilts, J., Chen, G. & Hughey, J. J. Evidence for widespread dysregulation of circadian clock progression in human cancer. *PeerJ* **6**, e4327 (2018).
41. Kelleher, F. C., Rao, A. & Maguire, A. Circadian molecular clocks and cancer. *Cancer Lett.* **342**, 9–18 (2014).
42. Brunton, S. L., Proctor, J. L. & Kutz, J. N. Discovering governing equations from data by sparse identification of nonlinear dynamical systems. *Proc. Natl Acad. Sci. USA* **113**, 3932–3937 (2016).
43. Soroldoni, D. et al. Genetic oscillations. A Doppler effect in embryonic pattern formation. *Science* **345**, 222–225 (2014).

Acknowledgements

We thank R. Cannavo for engineering the U2OS-Dual cell line and J. Bieler for initial analyses. We also thank F. Kuttler from the EPFL Biomolecular Screening Facility and L. Bozzo and J. Artacho from the EPFL Bioimaging and Optics Core Facility for assistance with the imaging. Fluorescence-activated cell sorting was performed at the EPFL Flow Cytometry Core Facility. This work was supported by the Swiss National Science Foundation grant 3100030_173079 and the EPFL. E.R.P. was supported by a Canadian Institute of Health Research (CIHR 358808) and a SystemsX.ch Transition Postdoc Fellowship (51FSP0163584).

Author contributions

C.D., E.R.P. and F.N. designed and participated in the study concept. C.D. and E.R.P. developed computational analysis tools. E.R.P. performed the experiments. C.D. and E.R.P. processed and analysed the experimental data. C.D., E.R.P. and F.N. interpreted the results. E.R.P. and F.N. acquired the funding. F.N. supervised the study. C.D., E.R.P. and F.N. wrote the manuscript.

Competing interests

The authors declare no competing interests.

Additional information

Supplementary information is available for this paper at <https://doi.org/10.1038/s41567-019-0598-1>.

Reprints and permissions information is available at www.nature.com/reprints.

Correspondence and requests for materials should be addressed to F.N.

Peer review information: *Nature Physics* thanks Mogens Jensen, Joris Pajjmans and the other, anonymous, reviewer(s) for their contribution to the peer review of this work.

Publisher's note: Springer Nature remains neutral with regard to jurisdictional claims in published maps and institutional affiliations.

© The Author(s), under exclusive licence to Springer Nature Limited 2019

Methods

Cell lines. All cell lines (U2OS-Dual, NIH3T3-Bmal1-Luc and U2OS-PGK-Luc) were maintained in a humidified incubator at 37°C with 5% CO₂ using DMEM cell culture medium supplemented with 10% fetal bovine serum (FBS) and 1% penicillin–streptomycin–glutamine (PSG). One day before luminescence or fluorescence acquisitions, we replaced DMEM with FluoroBrite DMEM media supplemented with 10% FBS and 1% PSG. NIH3T3 perturbation experiments were generated in Bieler et al.⁵. Briefly, they correspond to temperature changes (34, 37 and 40°C), treatment with CDK1 (RO-3306, Sigma-Aldrich) and CDK1/2 (NU-6102, Calbiochem) inhibitors at 1, 5, 7 and 10 μM [CDK1in-[1,5,7,10] and CDK2in-[1,5,7,10]], and short hairpin RNA-mediated knockdown of Cry2.

Fluorescent time-lapse microscopy. Time-lapse fluorescent microscopy for U2OS-Dual cells was performed at the Biomolecular Screening Facility (Swiss Federal Institute of Technology (EPFL)) using an InCell Analyzer 2200 (GE Healthcare). Experiments were performed at different temperatures (34°C, 37°C or 40°C) with a humidity and CO₂ (5%) control system. We used 100 ms excitation at 513/17 nm and emission at 548/22 nm to record the YFP channel. Cells were recorded by acquiring one field of view per well in a 96-well black plate (GE Healthcare). We used our previously developed semi-automated pipeline for segmentation and tracking of individual cells⁵. In total, traces from $n = 551$ U2OS cells were obtained (typically 50 cells are obtained per video). NIH3T3 single-cell traces are reanalysed from previous work⁵; here, we used $n = 2,504$ of those time traces. In all cases (NIH3T3 and U2OS), we followed several quality control metrics from ref. ⁵. Briefly, we discarded all traces that left the field of view at some point during the acquisition. We also visually inspected all traces, using a custom-made Matlab tool, to remove traces with problematic segmentation and tracking. In addition, we kept only traces with significant circadian amplitude (peak height >0.25, rescaled signals, Supplementary Information). To minimize boundary artefacts, typically, only traces with at least two full cell cycles were kept. The number of cells used for specific analyses, including sub-selections of traces based on the cell-cycle intervals, are indicated in the figure captions.

Inferring the phase dynamics of two biological oscillators. Denoted by D the entire set of single-cell traces comprising temporal intensity measurements ($\Delta t = 30$ min) from all fluorescent traces and Λ the set of model parameters, comprising the gridded coupling function F_{ij} . Note that all parameters are shared by all cells in D . To reconstruct the phase dynamics of our model, we seek to maximize the likelihood of the data $\mathcal{L}(\Lambda|D)$; that is, we solve:

$$\Lambda^* = \text{argmax } \mathcal{L}(\Lambda|D)$$

In practice, we used an expectation–maximization algorithm, by iteratively optimizing the function $Q(\Lambda, \Lambda')$ over its first argument, where Q can be written as follows:

$$Q(\Lambda, \Lambda') = E[\log p(D, \mathbf{X}|\Lambda)|\mathbf{X}, \Lambda']$$

That is, $Q(\Lambda, \Lambda')$ corresponds to the expected value of the log-likelihood of the data with respect to the posterior probabilities of the hidden phases \mathbf{X} (latent variables), computed using the current parameter Λ' . This process guarantees a monotonous convergence of the log-likelihood, although a global maximum is not necessarily reached⁴⁴.

To control for the many parameters F_{ij} , we added regularization constraints for both the smoothness and sparsity:

$$Q_p(\Lambda, \Lambda') = Q(\Lambda, \Lambda') - \lambda_1 \sum_{ij} ||\nabla F_{ij}||^2 - \lambda_2 \sum_{ij} F_{ij}^2$$

This expression is also guaranteed to converge⁴⁵.

Details about the optimization method, choice of the regularization parameters and computation of the phase posteriors using a HMM are provided in the Supplementary Information.

Long-term temperature entrainment and luminescence recording. We performed long-term temperature entrainment experiments using a Tecan plate reader Infinite F200 pro with CO₂ and temperature modules. One day before starting the experiment, serial dilutions ranging from 40,000 to 2,500 cells were seeded in 96-well white flat-bottom plates (Costar 3917). To prevent medium evaporation, all wells were filled with 300 μl of medium composed of FluoroBrite, 10% FBS, 1% PSG and 100 nM d-luciferin (NanoLight Technology) and covered with a sealing tape (Costar 6524). We set up temperature entrainment using a stepwise increase (or decrease) of 0.5°C every 2 h to produce temperature-oscillating profiles going from 35.5°C to 38.5°C and back to 35.5°C again over a period of 24 h. Intensities from all wells were recorded every 10 min with an integration time of 5,000 ms. Since temperature impacts the enzymatic activity of the luciferase⁴⁶, we corrected the signal for this systematic effect (Supplementary Information).

Association between gene expression and phase in tissues. We used the average gene expression obtained from a selected set of 12 adult (6-week-old males) mouse tissues from the Zhang et al. dataset (GEO accession GSE54650)²⁶. For this analysis, we estimated the Pearson correlation between the averaged gene expression and the circadian tissue phases or amplitudes reported in ref. ²⁷. We selected the top 200 genes positively or negatively associated with either the phases or the amplitudes for gene ontology analysis⁴⁷ (Supplementary Table 1).

Reporting Summary. Further information on research design is available in the Nature Research Reporting Summary linked to this article.

Data availability

The data supporting the figures and other findings of this study are available from the corresponding author on request.

Code availability

The code is available at <https://c4science.ch/diffusion/9123/>.

References

44. Dempster, A. P., Laird, N. M. & Rubin, D. B. Maximum likelihood from incomplete data via the EM algorithm. *J. R. Stat. Soc. Ser. B* **39**, 1–38 (1977).
45. Green, P. J. On use of the EM for penalized likelihood estimation. *J. R. Stat. Soc. Ser. B* **52**, 443–452 (1990).
46. Koksharov, M. I. & Ugarova, N. N. Approaches to engineer stability of beetle luciferases. *Comput. Struct. Biotechnol. J.* **2**, e201209004 (2012).
47. Huang da, W., Sherman, B. T. & Lempicki, R. A. Bioinformatics enrichment tools: paths toward the comprehensive functional analysis of large gene lists. *Nucleic Acids Res.* **37**, 1–13 (2009).

Reporting Summary

Nature Research wishes to improve the reproducibility of the work that we publish. This form provides structure for consistency and transparency in reporting. For further information on Nature Research policies, see [Authors & Referees](#) and the [Editorial Policy Checklist](#).

Statistics

For all statistical analyses, confirm that the following items are present in the figure legend, table legend, main text, or Methods section.

n/a Confirmed

- The exact sample size (n) for each experimental group/condition, given as a discrete number and unit of measurement
- A statement on whether measurements were taken from distinct samples or whether the same sample was measured repeatedly
- The statistical test(s) used AND whether they are one- or two-sided
Only common tests should be described solely by name; describe more complex techniques in the Methods section.
- A description of all covariates tested
- A description of any assumptions or corrections, such as tests of normality and adjustment for multiple comparisons
- A full description of the statistical parameters including central tendency (e.g. means) or other basic estimates (e.g. regression coefficient) AND variation (e.g. standard deviation) or associated estimates of uncertainty (e.g. confidence intervals)
- For null hypothesis testing, the test statistic (e.g. F , t , r) with confidence intervals, effect sizes, degrees of freedom and P value noted
Give P values as exact values whenever suitable.
- For Bayesian analysis, information on the choice of priors and Markov chain Monte Carlo settings
- For hierarchical and complex designs, identification of the appropriate level for tests and full reporting of outcomes
- Estimates of effect sizes (e.g. Cohen's d , Pearson's r), indicating how they were calculated

Our web collection on [statistics for biologists](#) contains articles on many of the points above.

Software and code

Policy information about [availability of computer code](#)

Data collection

All fluorescent movies were acquired using the GE In Cell Investigator v1.5 software. All luminescence experiments were acquired using the Tecan i-control v1.10.4.0 software.

Data analysis

All segmentation and tracking were performed using our custom-made pipeline (<https://github.com/jonathanBieler/segmentation>) using Matlab vR2016b. All analyses related to the reconstruction of the coupling functions and downstream analyses were performed with Python v3.5.2 (Anaconda v4.2.0). All the analysis related to the conservation of the coupling from mouse to human, the temperature entrainment experiments, and the expression of proliferation genes in tissue-specific circadian phases were performed with R v3.5.2. As stated in the main text in our Code availability statement, the code is available online at the following URL:
<https://github.com/ColasDroin/CouplingHMM>

For manuscripts utilizing custom algorithms or software that are central to the research but not yet described in published literature, software must be made available to editors/reviewers. We strongly encourage code deposition in a community repository (e.g. GitHub). See the Nature Research [guidelines for submitting code & software](#) for further information.

Data

Policy information about [availability of data](#)

All manuscripts must include a [data availability statement](#). This statement should provide the following information, where applicable:

- Accession codes, unique identifiers, or web links for publicly available datasets
- A list of figures that have associated raw data
- A description of any restrictions on data availability

The data supporting figures and other findings of this study are available from the corresponding author on request.

Field-specific reporting

Please select the one below that is the best fit for your research. If you are not sure, read the appropriate sections before making your selection.

- Life sciences Behavioural & social sciences Ecological, evolutionary & environmental sciences

For a reference copy of the document with all sections, see nature.com/documents/nr-reporting-summary-flat.pdf

Life sciences study design

All studies must disclose on these points even when the disclosure is negative.

Sample size	We used a total of n=2504 and n=551 time-lapse microscopy cell traces for NIH3T3 and U2OS, respectively. Each trace was imaged at a sampling rate of 30 min for at least 48 hours (>96 time points per trace). While developing the reconstruction method for the coupling function F, we assessed the dependency of the optimal solution in function of the number of cells, which is tightly linked with the regularization scheme described in details in the Supplementary Information.
Data exclusions	We followed several quality control metrics from our previous publication (Bieler et al. MSB 2014). Briefly, we discarded all traces that left the field-of-view at some point during the acquisition. We also visually inspected all traces, using a custom-made Matlab tool, to remove traces with problematic segmentation and tracking. Moreover, we only kept traces with significant circadian amplitude (peak height >0.25 of rescaled signals).
Replication	The collection for time-lapse cell traces are extracted from multiple movies in different wells (typically 50 cells can be obtained from one movie) and plates prepared and acquired on different days. All conditions (temperature and cell types) used a minimum of 5 independent wells or movies.
Randomization	N/A
Blinding	N/A

Reporting for specific materials, systems and methods

We require information from authors about some types of materials, experimental systems and methods used in many studies. Here, indicate whether each material, system or method listed is relevant to your study. If you are not sure if a list item applies to your research, read the appropriate section before selecting a response.

Materials & experimental systems		Methods	
n/a	Involved in the study	n/a	Involved in the study
<input checked="" type="checkbox"/>	<input type="checkbox"/> Antibodies	<input checked="" type="checkbox"/>	<input type="checkbox"/> ChIP-seq
<input type="checkbox"/>	<input checked="" type="checkbox"/> Eukaryotic cell lines	<input checked="" type="checkbox"/>	<input type="checkbox"/> Flow cytometry
<input checked="" type="checkbox"/>	<input type="checkbox"/> Palaeontology	<input checked="" type="checkbox"/>	<input type="checkbox"/> MRI-based neuroimaging
<input checked="" type="checkbox"/>	<input type="checkbox"/> Animals and other organisms		
<input checked="" type="checkbox"/>	<input type="checkbox"/> Human research participants		
<input checked="" type="checkbox"/>	<input type="checkbox"/> Clinical data		

Eukaryotic cell lines

Policy information about [cell lines](#)

Cell line source(s)	The NIH3T3 and U2OS cells were obtained from Dr Ueli Schibler (Department of Molecular Biology, Université de Genève) and Dr David Gadfield (Center for Integrative Genomics, Université de Lausanne), respectively.
Authentication	The NIH3T3 and U2OS cell lines were tested for circadian rhythmicity but not authenticated further.
Mycoplasma contamination	All cell lines are mycoplasma free as tested using the MycoAlert mycoplasma detection kit (Lonza).
Commonly misidentified lines (See ICLAC register)	Name any commonly misidentified cell lines used in the study and provide a rationale for their use.